

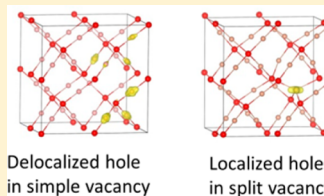
# Electronic Structure of Pure and Doped Cuprous Oxide with Copper Vacancies: Suppression of Trap States

Leah Y. Isseroff<sup>†</sup> and Emily A. Carter<sup>\*§</sup>

<sup>†</sup>Departments of Chemical and Biological Engineering and <sup>§</sup>Mechanical and Aerospace Engineering, Program in Applied and Computational Mathematics, and Andlinger Center for Energy and the Environment, Princeton University, Princeton, New Jersey 08544-5263, United States

Supporting Information

**ABSTRACT:** Cuprous oxide ( $\text{Cu}_2\text{O}$ ) is an attractive material for solar energy applications, but its photoconductivity is limited by minority carrier recombination caused by native defect trap states. We examine the creation of trap states by cation vacancies, using first principles calculations based on density functional theory (DFT) to analyze the electronic structure and calculate formation energies. With several DFT-based methods, a simple vacancy is predicted to be consistently more stable than a split vacancy by  $0.21 \pm 0.03$  eV. Hybrid DFT is used to analyze the density of states and charge density distribution, predicting a delocalized hole for the simple vacancy and a localized hole for the split vacancy, in contrast to previously reported results. The differing character of the two defects indicates that they contribute to conduction via different mechanisms, with the split vacancy as the origin of the acceptor states that trap minority carriers. We explore methods of improving photoconductivity by doping  $\text{Cu}_2\text{O}$  with Li, Mg, Mn, and Zn, analyzing their impact on vacancy formation energies and electronic structures. Results suggest that the Li dopant has the greatest potential to improve the photoconductivity of the oxide by inhibiting the creation of trap states.



**KEYWORDS:**  $\text{Cu}_2\text{O}$ , vacancy formation energy, trap states, doping, density functional theory, solar energy, photoconductivity

## 1. INTRODUCTION

Cuprous oxide ( $\text{Cu}_2\text{O}$ ) is a p-type semiconductor with promising potential as a low-cost material for photovoltaic and photocatalytic applications. It is nontoxic and abundant, and its band gap of 2.17 eV makes it an excellent candidate for solar energy technologies.<sup>1</sup> However,  $\text{Cu}_2\text{O}$  heterojunction solar cells have achieved only low efficiencies of up to 2%,<sup>2</sup> and the use of  $\text{Cu}_2\text{O}$  in photocatalytic water splitting has had limited success.<sup>3,4</sup> One cause of these low efficiencies is the reduction of photoconductivity due to carrier recombination in the bulk. Intrinsic defects in  $\text{Cu}_2\text{O}$  create trap states that inhibit minority carrier diffusion, resulting in a lower effective photocurrent.<sup>5</sup> Discovering methods to prevent trap state formation will improve  $\text{Cu}_2\text{O}$  photoconductivity and its performance in solar energy applications. To do so, it is first necessary to gain a better understanding of the electronic structure of intrinsic defects in  $\text{Cu}_2\text{O}$  and how they affect the conduction mechanism.

It has been established experimentally<sup>6–10</sup> and theoretically<sup>11–14</sup> that at higher oxygen pressures (such as ambient conditions), the dominant contributors to the p-type character of  $\text{Cu}_2\text{O}$  are Cu vacancies. Consequently, our study focuses on cation vacancies only, as opposed to other native defects, and their effect on the electronic structure. Cu vacancies are intrinsic defects that naturally occur in p-type  $\text{Cu}_2\text{O}$ , with a vacancy concentration range of  $1 \times 10^{18}$  to  $1 \times 10^{19} \text{ cm}^{-3}$ , varying with oxygen pressure.<sup>15</sup> Two types of single cation vacancies have been proposed: the simple vacancy, denoted  $V_{\text{Cu}}$  and the split vacancy, denoted  $V_{\text{Cu}}^{\text{split}}$ .  $V_{\text{Cu}}$  is created by the

removal of a single Cu atom, leaving behind two triply coordinated O atoms.  $V_{\text{Cu}}^{\text{split}}$  is formed when a nearby Cu atom moves toward the simple vacancy site, resting in a stable intermediate state, where it achieves tetrahedral coordination to four O atoms.

Experimental studies of  $\text{Cu}_2\text{O}$  have helped characterize Cu vacancies. Experimentally derived vacancy formation enthalpies (VFEs) range from 0.39 to 0.97 eV/defect.<sup>7–10,16,17</sup> This scatter in the data exists because of varying oxygen pressures, as well as some observed dependence of formation enthalpy on temperature.<sup>7</sup> Additionally, absorption and photoconductivity spectra feature an acceptor energy band at 0.55–0.61 eV above the valence band maximum (VBM) that has been attributed to Cu vacancies.<sup>15</sup> The dependence of dark conductivity on temperature has also been used to characterize intrinsic defects. Conductivity in  $\text{Cu}_2\text{O}$  exhibits an Arrhenius dependence on temperature. For lower temperatures at which new defects do not easily form and the concentration of defects may be considered to be fixed, the only contribution to the activation energy associated with conduction will be the acceptor ionization energy. O'Keeffe and Moore found three different temperature ranges in which each was characterized by a different activation energy, with a low temperature activation energy (and corresponding acceptor ionization energy) of 0.6 eV.<sup>18</sup> Work by Brattain showed that  $\text{Cu}_2\text{O}$  is a charge-

**Received:** April 30, 2012

**Revised:** January 9, 2013

**Published:** January 9, 2013

compensated material, with a predicted acceptor level at about 0.3 eV above the valence band.<sup>19</sup> However, these simple models with a single acceptor band do not fully represent the complex electrical properties of Cu<sub>2</sub>O. The activation energy for conductivity also depends strongly on the conditions of preparation. Specifically, there is a linear relationship between the activation energy and the logarithm of the annealing temperature,<sup>20</sup> which is a manifestation of the Meyer-Neldel rule.<sup>21</sup> To explain this behavior, an electronic model was proposed with a band of acceptor levels in the gap as opposed to a single acceptor level.<sup>22</sup> By annealing the sample at a specific temperature, a unique internal arrangement of defects is fixed in the crystal, in addition to a specific compensation ratio, resulting in a distinct activation energy at each annealing temperature. Additional electronic models exist based on multiple interpretations of the phenomenon of persistent photoconductivity, or photomemory.<sup>23–28</sup> In sum, no single complete electronic model accurately describes all phenomena in Cu<sub>2</sub>O conductivity, and ambiguity persists in the relationship between the energetics of intrinsic defect states and conductivity.

Cu vacancies in Cu<sub>2</sub>O have also been the focus of numerous theoretical studies. Wright and Nelson used density functional theory (DFT) with the local density approximation for exchange-correlation (XC) to calculate VFEs, finding that V<sub>Cu</sub> was less stable than V<sub>Cu</sub><sup>split</sup> by 0.1 eV.<sup>29</sup> The electronic structure of these defects was not analyzed. A number of other DFT studies used a generalized gradient approximation (GGA) for XC, finding conversely that V<sub>Cu</sub> was more stable than V<sub>Cu</sub><sup>split</sup>.<sup>11–13,30</sup> Raebiger et al.<sup>12</sup> used DFT-GGA with a set of *a posteriori* corrections as outlined by Persson et al.,<sup>31</sup> adding a rigid shift—derived from GGA+U calculations—to the VBM, which may introduce inaccuracies in all level positions. They predicted  $\Delta H_f(V_{\text{Cu}}) = 0.7$  eV and  $\Delta H_f(V_{\text{Cu}}^{\text{split}}) = 1.0$  eV. Soon et al. used DFT-GGA with no corrections, finding the same energy difference as Raebiger et al., but with lower VFEs:  $\Delta H_f(V_{\text{Cu}}) = 0.47$  eV and  $\Delta H_f(V_{\text{Cu}}^{\text{split}}) = 0.78$  eV. Scanlon et al. found a larger difference with DFT-GGA:  $\Delta H_f(V_{\text{Cu}}) = 0.41$  eV and  $\Delta H_f(V_{\text{Cu}}^{\text{split}}) = 1.24$  eV. Finally, Nolan and Elliot reported the smallest difference in VFEs, also using DFT-GGA:  $\Delta H_f(V_{\text{Cu}}) = 0.41$  eV and  $\Delta H_f(V_{\text{Cu}}^{\text{split}}) = 0.47$  eV. Although all of these studies used the same GGA functional, a wide range of values was produced for the VFEs and their relative magnitude. These differences likely stem from varying computational parameters and cell structures, illustrating the importance of testing all parameters for convergence to ensure overall accuracy. In spite of their differences, all DFT-GGA studies found that the hole existed as a delocalized band crossing the Fermi level, predicting semimetallic behavior for both types of vacancies. This conflicts with the experimental observation of activated p-type semiconduction in Cu<sub>2</sub>O marked by the Arrhenius dependence of conduction on temperature, which is indicative of localized defect states in the gap. This contradiction implies that DFT-GGA does not accurately model these vacancies and that one needs to go beyond standard DFT for a reliable description of this material.

An alternative to the standard DFT approach is DFT+U,<sup>32,33</sup> which introduces a parametrized Hartree-Fock (HF) potential (with one parameter, U–J) to describe on-site Coulomb (U) and exchange (J) interactions of highly localized electrons. GGA+U was used by Nolan and Elliot with a U–J value of 7 eV, resulting in  $\Delta H_f(V_{\text{Cu}}) = 1.17$  eV and  $\Delta H_f(V_{\text{Cu}}^{\text{split}}) = 1.70$  eV.<sup>30</sup> They found that the hole remained delocalized for both

types of vacancies. However, Scanlon et al. used GGA+U ( $U-J = 5.2$  eV) and found that although the simple vacancy remained notionally metallic, the hole exhibited polaronic character in the split vacancy.<sup>13</sup> They reported a slightly larger energy difference than Nolan and Elliot, with  $\Delta H_f(V_{\text{Cu}}) = 0.92$  eV and  $\Delta H_f(V_{\text{Cu}}^{\text{split}}) = 1.66$  eV. Despite its improved accuracy, Scanlon et al. rejected GGA+U as an accurate method due to its inability to reproduce experimental ionization levels.

Finally, Scanlon et al. used a screened hybrid DFT approach with the HSE XC functional,<sup>34–36</sup> and observed distinct single particle levels within the band gap for both types of vacancies.<sup>14</sup> The discrete levels indicate that the hole is localized in both defect types, agreeing with experimental expectations. Based on these results, in addition to good agreement between transition level calculations and experimental ionization levels, they maintained that the HSE functional is needed to reproduce the correct physics of Cu<sub>2</sub>O cation vacancies. However, the conclusions of Scanlon et al. may be suspect because only the gamma point was sampled for Brillouin zone integration (presumably due to computational limitations at the time the study was conducted). The limited k-point mesh can result in unconverged energies and will significantly impact the accuracy of the electronic structure. One indication of this is that their relative energies for VFEs differ significantly from all previous results. They reported  $\Delta H_f(V_{\text{Cu}}) = 1.15$  eV and  $\Delta H_f(V_{\text{Cu}}^{\text{split}}) = 1.14$  eV, indicating that V<sub>Cu</sub><sup>split</sup> is just slightly more stable than V<sub>Cu</sub>, in contrast with the much greater stability of V<sub>Cu</sub> in most DFT-GGA and GGA+U calculations. Now that more accurate calculations can be performed, it is crucial to sample a larger k-point mesh to verify the accuracy of such predictions, as proper sampling could lead to dramatic changes in the electronic structure, which might overturn previously established conclusions.

Because of the inconsistencies in published theoretical work, we believe it is necessary to revisit DFT-based calculations of Cu vacancies in Cu<sub>2</sub>O. Here we aim to resolve the lack of clarity regarding VFEs and relative stabilities, as well as to gain a better understanding of the electronic structure of vacancies. We study the extent of hole localization in these defects, using the Bader method as a tool for quantitative analysis of the charge distribution.<sup>37</sup> Finally, to design ways to counteract the negative impact these defects have on photoconductivity, we also investigate how substitutional cation doping can be used to improve electronic properties.

Cu<sub>2</sub>O has been doped to modify its optical and electronic properties for other applications.<sup>38–40</sup> Nolan and Elliot used DFT-GGA to study substitutional cation doping of Cu<sub>2</sub>O, aiming to enable Cu<sub>2</sub>O to be used as a transparent conducting oxide by increasing its band gap.<sup>39,40</sup> They postulated that introducing dopants that cause large structural distortions would disrupt Cu–Cu interactions, thereby opening up the band gap. They used the Perdew-Burke-Ernzerhof (PBE)<sup>41,42</sup> GGA XC functional, and although it significantly underestimates the band gap, it can be used to observe trends in the effect of dopants on VFEs and band gaps. They found that the impact of the dopant depended on its ionic radius, its oxidation state, and the detailed electronic structure of the dopant and the host. Substitution by cations with a larger ionic radius led to lower VFEs, but the effect on the gap was mainly dependent on the alignment of dopant electronic states with Cu<sub>2</sub>O band edges and the extent of their hybridization. The effect of doping on conductivity could not be properly analyzed because DFT-

PBE predicts that the hole is delocalized in both undoped and doped Cu<sub>2</sub>O.

The conclusions of Nolan and Elliot help to define a set of design criteria when choosing dopants for our application to enhance photoconductivity. First, substitutional cations should have similar ionic radii to Cu<sup>+</sup> in order to minimize structural distortion. (We do not want to alter the band gap, in contrast to Nolan and Elliot.) Additionally, although a detailed study of the electronic structure is necessary to determine the true impact of the dopant on the density of states (DOS), dopants with a closed shell or a  $d^5$  electron configuration should be less likely to form trap states due to their inherent stability.<sup>43</sup> Ideally, we wish to select dopants that are nontoxic, abundant, and soluble in Cu<sub>2</sub>O, even if only to a low percentage. We chose to study both aliovalent and isovalent dopants, to be able analyze the effect of a compensatory electron on the formation of the first vacancy. On the basis of these criteria, the dopants studied in this work are Li, Mg, Mn, and Zn, whose ionic radii are comparable to Cu<sup>+</sup> (see the Supporting Information, Table S1).<sup>44</sup>

Our approach uses PBE+U theory to relax doped and undoped Cu<sub>2</sub>O structures, because PBE+U reproduces the experimental structure of Cu<sub>2</sub>O in the stoichiometric unit cell.<sup>45</sup> After structure optimization, DFT-HSE is used for a detailed study of the electronic structure, as DFT-HSE generates the most accurate electronic structure in stoichiometric Cu<sub>2</sub>O.<sup>45</sup> The DOS is analyzed to identify the existence of trap states, first in undoped Cu<sub>2</sub>O containing a single Cu vacancy and then in doped Cu<sub>2</sub>O containing one or two Cu vacancies to discern the effect of the selected dopants on the electronic structure. Because the hole from the first vacancy is compensated by the additional electron from the aliovalent n-type dopants, the formation of a second vacancy and the resulting electronic structure are also studied in these cases. Although the DOS can be used to identify if the hole is localized or delocalized, Bader analysis is used as a more quantitative measure to evaluate the extent of hole localization. Previous results for undoped Cu<sub>2</sub>O are reexamined and reinterpreted, whereas doped nonstoichiometric Cu<sub>2</sub>O is assessed for the first time, revealing strategies to improve the conductive properties of Cu<sub>2</sub>O for photovoltaic and photocatalytic applications.

## 2. METHODS

The Vienna Ab-initio Simulation Package (VASP version 5.2.2)<sup>46</sup> was used to run all DFT-based calculations. Blöchl's all-electron, frozen-core projector augmented wave (PAW) method<sup>47</sup> was used to represent nuclei and core electrons (Cu[Ar], O[He], Li[He], Mg[Ne], Mn[Ar], and Zn[Ar], where the element in brackets represents the frozen core), and all PAW potentials were obtained from the VASP package, using the standard PAW potential for O. The PBE XC functional was used for DFT and DFT+U. The formalism of Dudarev et al.<sup>48</sup> was used for DFT+U with a U-J value of 6 eV, which was shown to be the optimal U-J value to reproduce the experimental structure.<sup>45</sup> For hybrid-DFT calculations with the HSE XC functional,<sup>34–36</sup> 25% of PBE exchange is replaced by screened nonlocal exact exchange, and the recommended value of 0.2 Å<sup>-1</sup> was used for the screening parameter.<sup>49</sup> 27.5% screened nonlocal exact exchange was also used in one calculation for V<sub>Cu</sub> in order to evaluate the effect of this mixing parameter and to compare to previously published results (*vide infra*).

The Cu<sub>2</sub>O unit cell comprises four Cu atoms and two O atoms arranged in the cuprite structure (space group Pn3m, No. 224). The (2 × 2 × 2) supercell of Cu<sub>2</sub>O was used to model single vacancies, corresponding to a vacancy concentration of ~3% when a single cation vacancy has been added and a dopant concentration of ~3% when a

single cation has been substituted by a dopant atom. This vacancy concentration corresponds to  $1 \times 10^{21} \text{ cm}^{-3}$ , which although greater than the experimental range can still be used to accurately calculate VFEs. Convergence of the VFEs with respect to supercell size was tested for calculations of  $\Delta H_f(V_{\text{Cu}})$  and  $\Delta H_f(V_{\text{Cu}}^{\text{split}})$  with PBE+U. It was found that using the larger (3 × 3 × 3) supercell resulted in a difference of only 0.01 eV for  $\Delta H_f(V_{\text{Cu}})$  and 0.06 eV for  $\Delta H_f(V_{\text{Cu}}^{\text{split}})$ , justifying the use of the smaller (2 × 2 × 2) cell for a single vacancy. The lattice constant for the supercell was fixed to 8.5476 Å, obtained from PBE+U calculations on the stoichiometric Cu<sub>2</sub>O unit cell. PBE+U was then used to relax all atomic positions, with a force convergence threshold of 0.03 eV Å<sup>-1</sup>.

The (3 × 3 × 3) supercell was used for initial PBE+U calculations of two Cu vacancies and one dopant atom, corresponding to respective vacancy and dopant concentrations of ~2% and ~1%. The lattice constant for this supercell was fixed at 12.8214 Å, and PBE+U was used to relax all atomic positions with the same force convergence threshold of 0.03 eV Å<sup>-1</sup>. The (2 × 2 × 2) supercell of Cu<sub>2</sub>O was also subsequently used to model two Cu vacancies and a dopant atom, corresponding to respective vacancy and dopant concentrations of ~6% and ~3%.

All bulk defect calculations in the (2 × 2 × 2) supercell used 280 bands and a planewave kinetic energy cutoff of 700 eV, which converged the total energy to within 1 meV/atom. All calculations were spin-polarized, with the total magnetization of the cell fixed to ensure that the hole is not split between the two spins, setting NUPDOWN = 1 for all materials other than when Mn is present; NUPDOWN = 4 is used for Mn<sup>2+</sup> to account for its high-spin, half-filled *d*-shell. The energy difference between states using an NUPDOWN of 4 or 6 for the Mn-doped cell with two vacancies was negligible, indicating that the hole is decoupled from the spin of the Mn *d* electrons (see the Supporting Information). The Brillouin zone was integrated using the tetrahedron method with Blöchl corrections.<sup>50</sup> For calculations using DFT-PBE and PBE+U, a 3 × 3 × 3 gamma-point-centered k-point mesh was used (14 irreducible k-points), which converged the total energy to within 1 meV/atom and the band gap to within 1 meV. For DFT-HSE, it was impossible to use the full 3 × 3 × 3 k-point mesh due to the large computational expense, so a 2 × 2 × 2 gamma-point-centered k-point mesh was used (eight irreducible k-points, including the gamma point). There was no down-sampling of the q-point mesh, which is the subset of k-points upon which the HF kernel is evaluated. Bulk calculations in the (3 × 3 × 3) supercell used a 2 × 2 × 2 gamma-point-centered k-point mesh and 840 bands. All other parameters were the same as in the smaller supercell.

The formation enthalpy of a neutral defect,  $\Delta H_f(D)$ , is defined as

$$\Delta H_f(D) = E(D) - E^H + \sum_i n_i(\mu_i^{\text{elem}} + \Delta\mu_i) \quad (1)$$

where  $E(D)$  is the total energy of the defective cell and  $E^H$  is the total energy of the stoichiometric host cell.  $\mu_i^{\text{elem}}$  are elemental reference energies of the constituent atoms in their standard states (i.e., O<sub>2</sub>(g) and Cu(s)), and  $\mu_i = \mu_i^{\text{elem}} + \Delta\mu_i$  is the chemical potential of a reservoir of atoms *i*, reflecting the specific equilibrium growth conditions.  $n_i$  is the number of constituent atoms removed from (added to) the host cell to create the defect, then formally added to (removed from) the external reservoir. Zero point energy (ZPE) contributions from the solids have been neglected based on the assumption that creating a vacancy does not significantly change the vibrational frequencies of the solids.

There are a number of thermodynamic limits to the chemical potentials  $\mu_{\text{Cu}}$  and  $\mu_{\text{O}}$ . To avoid precipitation of metallic Cu and the formation of molecular O<sub>2</sub>, the chemical potential of the atoms in the reservoir must be lower than the elemental reference energies, such that

$$\begin{aligned} \Delta\mu_{\text{Cu}} &\leq 0, \\ \Delta\mu_{\text{O}} &\leq 0 \end{aligned} \quad (2)$$

To avoid the formation of the secondary solid CuO, the chemical potentials must also be bounded by

$$\begin{aligned} \mu_{\text{Cu}} + \mu_{\text{O}} &\leq \mu_{\text{CuO}}, \\ \text{or } \Delta\mu_{\text{Cu}} + \Delta\mu_{\text{O}} &\leq \Delta H_f(\text{CuO}) \end{aligned} \quad (3)$$

Finally, to maintain thermodynamic equilibrium with Cu<sub>2</sub>O, chemical potentials  $\mu_{\text{Cu}}$  and  $\mu_{\text{O}}$  are constrained by the equilibrium condition;

$$\begin{aligned} 2\mu_{\text{Cu}} + \mu_{\text{O}} &= \mu_{\text{Cu}_2\text{O}}, \\ \text{or } 2\Delta\mu_{\text{Cu}} + \Delta\mu_{\text{O}} &= \Delta H_f(\text{Cu}_2\text{O}) \end{aligned} \quad (4)$$

The upper bound to  $\mu_{\text{Cu}}$  corresponds to a maximally Cu-rich/O-poor environment, and the lower bound corresponds to a Cu-poor/O-rich environment. In this work, formation enthalpies and elemental reference energies are calculated from first principles, keeping the XC functional consistent in all parts of the calculation that contribute to eq 1.

The reference energy for Cu was calculated using a four-atom fcc unit cell, with a gamma-point-centered  $16 \times 16 \times 16$  k-point mesh (2052 irreducible k-points) and a planewave kinetic energy cutoff of 700 eV. In order to be computationally feasible, DFT-HSE calculations used an  $12 \times 12 \times 12$  k-point mesh with a down-sampled  $4 \times 4 \times 4$  q-point mesh for the HF kernel, which converged the energy to within 0.1 eV/atom for the q-point mesh and 0.01 eV/atom for the k-point mesh. The Brillouin zone was integrated using Methfessel-Paxton smearing (with the recommended smearing width of 0.2 eV) when optimizing the cell volume, but the tetrahedron method with Blöchl corrections was used to obtain final energies. The equilibrium lattice constant was optimized with each XC functional, converged to a force threshold of 0.03 eV Å<sup>-1</sup>. The use of each XC functional was justified by evaluating its ability to reproduce the experimental lattice constant and bulk modulus of Cu metal, shown in Table 1. The results show

**Table 1. Lattice Constant and Bulk Modulus for Cu Metal, Calculated with DFT-PBE, PBE+U, and DFT-HSE, Compared to Experiment (at 298 K)**

	lattice constant (Å)	bulk modulus (GPa)
DFT-PBE	3.637	137
PBE+U	3.603	115
DFT-HSE	3.643	126
Exp.	3.615 <sup>56</sup>	138 <sup>57</sup>

that all functionals predict lattice constants within <0.8% of experiment. However, the accuracy in calculating the bulk modulus varied: the DFT-PBE value is within 0.6% of experiment, whereas DFT-HSE and PBE+U underestimate the experimental value by 8 and 17%, respectively.

The reference energy for O was calculated by modeling the  $^3\Sigma_g^-$  ground state of O<sub>2</sub> (spin-polarized DFT used for open-shell systems produces eigenfunctions of  $\hat{S}_z$  but not  $\hat{S}^2$ ; therefore the DFT description of O<sub>2</sub> is not quite the true triplet). The planewave kinetic energy cutoff was 900 eV, and Brillouin zone integration (over a single k-point) employed Gaussian smearing with a smearing width of 0.0001 eV for one O<sub>2</sub> molecule isolated in an orthorhombic periodic cell with lattice vectors 9.0, 9.1, and 9.2 Å. The bond length was optimized with each XC functional, resulting in a bond length of 1.232 Å with DFT-PBE (and PBE+U) and 1.210 Å with DFT-HSE, reproducing the experimental bond length of 1.21 Å.<sup>51</sup>

Total energies of Cu<sub>2</sub>O and CuO were calculated using the unit cell for each material. Computational details used for Cu<sub>2</sub>O are provided in ref 45. The CuO unit cell is monoclinic, belonging to the space group C2/c (No. 15). It contains four Cu atoms and four O atoms. CuO calculations used the same parameters as those for Cu<sub>2</sub>O, but with a gamma-point-centered k-point mesh of  $8 \times 6 \times 8$  and 40 bands, which converged the total energy to within 0.001 eV/formula unit. All structures (lattice vectors and ion positions) were optimized with each XC functional.

Elemental reference energies and the formation energies of CuO and Cu<sub>2</sub>O are reported in Table 2. The calculated formation enthalpies

**Table 2. Elemental Reference Energies (eV/atom)<sup>a</sup> and Cu<sub>2</sub>O and CuO Zero Kelvin Formation Enthalpies (eV/formula unit), Calculated with DFT-PBE, PBE+U, and DFT-HSE, compared to Experiment (at 298.15 K)**

	$\mu_{\text{Cu}}^{\text{elem}}$	$\mu_{\text{O}}^{\text{elem}}$	$\Delta H_f(\text{Cu}_2\text{O})$	$\Delta H_f(\text{CuO})$
DFT-PBE	-3.718	-4.889	-1.276	-1.225
PBE+U	-1.751	-4.889	-1.643	-1.205
DFT-HSE	-4.066	-8.468	-1.623	-1.438
Exp.			-1.75 <sup>51</sup>	-1.63 <sup>51</sup>

<sup>a</sup>Only the elemental reference energy for O includes contributions from the ZPE. We assume that the ZPEs from the solid phases will cancel in formation energy calculations; however, we include the ZPE contribution in the oxygen reference energy because the O<sub>2</sub> vibrational frequency is significantly larger than the frequencies present in the solids.

are significantly less negative than the experimental values of -1.63 eV for CuO and -1.75 eV for Cu<sub>2</sub>O,<sup>51</sup> which is in part due to the differing temperatures for calculation (0 K) and experiment (298.15 K). All three theories give the right qualitative trend (Cu<sub>2</sub>O more stable than CuO), but overall, DFT-HSE gives values in closest agreement with experiment. The values in Table 2 and the constraints set by eqs 2–4 allow for the bounds on the chemical potentials to be calculated, which are shown in Table 3. The chemical potentials for Cu are used to provide a range for cation vacancy formation energies, representing its dependence on experimental growth conditions.

**Table 3. Upper and Lower Bounds for Cu and O Chemical Potentials (eV/atom), Calculated with DFT-PBE, PBE+U, and DFT-HSE**

	Cu-rich/O-poor		Cu-poor/O-rich	
	$\Delta\mu_{\text{Cu}}$	$\Delta\mu_{\text{O}}$	$\Delta\mu_{\text{Cu}}$	$\Delta\mu_{\text{O}}$
DFT-PBE	0	-1.276	-0.051	-1.175
PBE+U	0	-1.642	-0.438	-0.767
DFT-HSE	0	-1.623	-0.185	-1.254

### 3. RESULTS AND DISCUSSION

**A. Simple and Split Vacancies in Pure Cu<sub>2</sub>O.** The structures for V<sub>Cu</sub> and V<sub>Cu</sub><sup>split</sup> were optimized with the PBE+U functional, and their stability as local minima was verified by ensuring that all vibrational frequencies were real (see the Supporting Information).

Using the PBE+U-optimized structures, VFEs were calculated with DFT-PBE, PBE+U, and DFT-HSE. These values, presented in Table 4, show that V<sub>Cu</sub> is consistently more stable than V<sub>Cu</sub><sup>split</sup> by  $0.21 \pm 0.03$  eV, regardless of environmental conditions or theoretical method. The DFT-PBE energies for V<sub>Cu</sub> and V<sub>Cu</sub><sup>split</sup> fall slightly below and within the lower limit of the experimental range for  $\Delta H_f(D)$  of 0.39–0.97 eV/defect. The PBE+U VFEs fall within the experimental range only under Cu-poor/O-rich conditions, showing the significant influence of experimental conditions and how they affect the chemical potential.  $\Delta\mu_{\text{Cu}}$  has a large range with PBE+U, and its effect on lowering  $\Delta H_f(D)$  to within the experimental range illustrates how VFEs can be extremely sensitive to the Cu chemical potential. Finally, VFEs for DFT-HSE are above the experimental range. Despite this inaccuracy, these values are still useful for studying relative trends for the effects of dopants

**Table 4. Cu Vacancy Formation Enthalpies at 0 K (VFEs, eV) for Simple and Split Vacancies in Undoped  $\text{Cu}_2\text{O}^a$**

	Cu-rich/O-poor		Cu-poor/O-rich	
	$V_{\text{Cu}}$	$V_{\text{Cu}}^{\text{split}}$	$V_{\text{Cu}}$	$V_{\text{Cu}}^{\text{split}}$
DFT-PBE	0.372	0.556	0.321	0.505
PBE+U	1.101	1.276	0.663	0.838
DFT-HSE	1.337	1.580	1.152	1.395
Exp.	0.39–0.97 <sup>7–10,16,17</sup>			

<sup>a</sup>VFEs for the two types of vacancies, as calculated with DFT-PBE, PBE+U, and DFT-HSE, according to eq 1 and using values from Tables 2 and 3 for elemental reference energies and the chemical potential ranges. All calculations are done on structures optimized with the PBE+U functional.

on  $\Delta H_f(D)$ , and the use of DFT-HSE is necessary to accurately study the electronic structure.

The energy difference between  $V_{\text{Cu}}$  and  $V_{\text{Cu}}^{\text{split}}$  remains fairly consistent regardless of the XC functional employed, especially in comparison to the range of reported relative energies in the literature. This consistency indicates that the choice of XC functional has a minimal effect on relative stability. The large range of energy differences reported in the literature is therefore a result of other differing variables, such as supercell size (directly related to the vacancy concentration), cell volume and structure, Brillouin zone integration, and various calculation parameters. This effect can be seen most significantly in the difference between our DFT-HSE energies and those reported by Scanlon et al.<sup>14</sup> Although both calculations use a 48-atom supercell and nearly the same percentage of local exchange in HSE, Scanlon et al. calculated that  $V_{\text{Cu}}^{\text{split}}$  is more stable than  $V_{\text{Cu}}$  by 0.01 eV, in contrast with our reported stability of  $V_{\text{Cu}}$  over  $V_{\text{Cu}}^{\text{split}}$  by 0.24 eV. Although many factors may contribute to this disparity, a significant influence is likely the different k-point meshes used for integrating over the Brillouin zone—their work sampled only the gamma point, whereas we used a gamma-point-centered  $2 \times 2 \times 2$  k-point and q-point mesh. The effect of k-point sampling on the electronic structure will be discussed further when analyzing the DOS.

When analyzing hole localization, a common approach is to plot the excess spin density. The DFT-HSE excess spin densities for both vacancy types are displayed in Figure 1. Both simple and split vacancies exhibit a degree of hole localization around the defect, although the hole density in  $V_{\text{Cu}}^{\text{split}}$  is strongly localized on the one Cu atom central to the defect whereas the hole density for  $V_{\text{Cu}}$  extends to a number of nearby atoms. While this visual representation is helpful for identifying the spatial extent of localization, it is ineffective in measuring the magnitude of localization. A quantitative evaluation of hole localization in DFT-HSE-derived charge densities can be accomplished with Bader analysis. Table 5 shows Bader charges averaged over the atom classes defined in Figure 2. The first column shows the Bader charges of Cu and O in stoichiometric bulk  $\text{Cu}_2\text{O}$ , presented so as to provide a basis on which to compare how charges change when a vacancy is introduced. Bader charges for  $V_{\text{Cu}}$  show small deviations from bulk charges with slight localization of the hole on nearby atoms  $\text{O}_{\text{NN}}$ ,  $\text{Cu}_{\text{NN}}$ , and  $\text{Cu}_{\text{NNN}}$ , but generally the hole is delocalized over all atoms. In  $V_{\text{Cu}}^{\text{split}}$ , the hole is almost entirely localized on  $\text{Cu}_s$ , the atom at the center of the defect. These Bader charges highlight how the magnitude of localization is much more significant for  $V_{\text{Cu}}^{\text{split}}$  than for  $V_{\text{Cu}}$ .

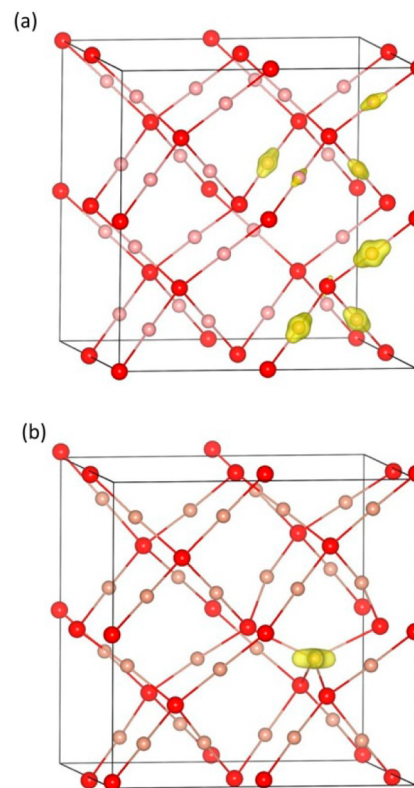


**Figure 1.** Excess spin density for undoped (a)  $V_{\text{Cu}}$  and (b)  $V_{\text{Cu}}^{\text{split}}$  in  $\text{Cu}_2\text{O}$ , as calculated with DFT-HSE. The red and pink spheres represent O and Cu, respectively. The isosurface level is set to half of the maximum density in each case, at  $0.014 \text{ e } \text{\AA}^{-3}$  for  $V_{\text{Cu}}$  and  $0.070 \text{ e } \text{\AA}^{-3}$  for  $V_{\text{Cu}}^{\text{split}}$ . The hole is quite delocalized for (a) the simple vacancy, whereas it is strongly localized for (b) the split vacancy.

**Table 5. Bader Charges for Simple and Split Vacancies<sup>a</sup>**

stoichiometric $\text{Cu}_2\text{O}$	$V_{\text{Cu}}$	$V_{\text{Cu}}^{\text{split}}$
$\text{O}_{\text{NN}}$		-1.07
$\text{O}_{\text{bulk}}$	-1.11	-1.11
$\text{Cu}_{\text{NN}}$		0.59
$\text{Cu}_{\text{NNN}}$		0.59
$\text{Cu}_{\text{bulk}}$	0.55	0.56
$\text{Cu}_s$		1.00

<sup>a</sup>Bader charges are presented averaged over classifications of atom types, as defined in Figure 2. The large positive charge on the Cu at the center of the split vacancy ( $\text{Cu}_s$ ) strongly implies hole localization.

The effect of hole localization on the electronic structure was further analyzed by plotting the DFT-HSE projected density of states (PDOS) for  $V_{\text{Cu}}$  and  $V_{\text{Cu}}^{\text{split}}$ , shown in comparison to the stoichiometric  $\text{Cu}_2\text{O}$  PDOS (Figure 3). The PDOS for stoichiometric  $\text{Cu}_2\text{O}$  in panel a shows that its band gap has no acceptor states within the gap, nor any states at the Fermi level. Panel b shows that  $V_{\text{Cu}}$  contains significant DOS at and immediately above the Fermi level, consistent with the creation of delocalized holes, but with no distinct acceptor states within the gap. This is in contrast with the PDOS of  $V_{\text{Cu}}^{\text{split}}$ , shown in panel c, which has a distinct peak at 0.57 eV above the Fermi level (shown in greater detail in the inset). Although a small DOS at and above the Fermi level also exists, it is negligible in comparison to the magnitude of the DOS at what is clearly a trap state.

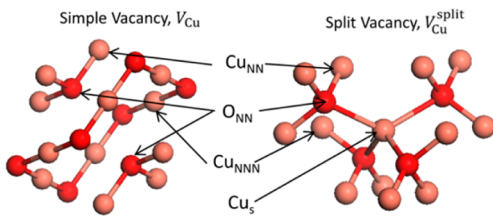


**Figure 2.** Local structures surrounding  $V_{\text{Cu}}$  and  $V_{\text{Cu}}^{\text{split}}$  in  $\text{Cu}_2\text{O}$ , identifying classifications of atom types as defined by their positions relative to the vacancy. For the split vacancy:  $\text{Cu}_s$  is the translated Cu that is at the center of the split vacancy;  $\text{O}_{\text{NN}}$  are the nearest neighbor O atoms to which  $\text{Cu}_s$  is tetrahedrally coordinated;  $\text{Cu}_{\text{NN}}$  are those Cu atoms nearest to  $\text{Cu}_s$  within 2.7 Å;  $\text{Cu}_{\text{NNN}}$  are those Cu atoms within 4 Å of  $\text{Cu}_s$ , excluding the  $\text{Cu}_{\text{NN}}$  atoms. For the simple vacancy, the definitions differ slightly:  $\text{O}_{\text{NN}}$  are the two O atoms between which the linearly coordinated Cu atom was removed to create the vacancy;  $\text{Cu}_{\text{NN}}$  are the Cu atoms coordinated to  $\text{O}_{\text{NN}}$ ;  $\text{Cu}_{\text{NNN}}$  are the Cu atoms in the other interlocking atomic network that encircle the defect, and are equidistant with  $\text{Cu}_{\text{NN}}$  to the vacancy.  $\text{O}_{\text{bulk}}$  and  $\text{Cu}_{\text{bulk}}$  are all other Cu and O atoms that are not included in the local structure.

The nature of the electronic structure as shown in the DFT-HSE DOS differs significantly from that described by Scanlon et al.,<sup>14</sup> who predicted no crossing through the Fermi level for either type of vacancy, and distinct single particle levels at 0.52 and 1.11 eV above the VBM for  $V_{\text{Cu}}$  and  $V_{\text{Cu}}^{\text{split}}$ , respectively. In order to identify the cause of this disparity, we reran our calculation for  $V_{\text{Cu}}$  keeping all computational parameters the same, but using a k-point mesh that sampled only the gamma point. This resulted in an electronic structure character similar to that of Scanlon et al., with no states at the Fermi level, and a single particle level within the gap at 0.46 eV above the VBM.

Additionally, to rule out the effect of the HSE mixing parameter choice, this same calculation was run with the mixing parameter value employed by Scanlon et al. of 27.5%, which exactly reproduced their results. These results indicate that the effect of the HSE mixing parameter is to slightly affect quantitative observations – shifting the peak by 0.06 eV – but qualitatively, the result is the same. Thus, it is an artifact of limited k-point sampling that hole localization was observed in the DOS of both vacancy structures. This highlights the importance of properly sampling the Brillouin zone, as insufficient k-point sampling in small supercells will lead to a drastically different conclusion about the nature of the electronic structure and the existence of trap states within the band gap. Sampling eight k-points instead of exclusively the gamma point results in a delocalized hole state for  $V_{\text{Cu}}$  illustrating that this defect creates a perturbed-host-state<sup>52</sup> in which there is no associated activation energy for p-type semiconduction. This is in contrast to the defect-localized-state<sup>52</sup> predicted with  $V_{\text{Cu}}^{\text{split}}$ , which will have an associated activation energy for initiating conductivity.

The differing electronic character evident in the DOS of  $V_{\text{Cu}}$  and  $V_{\text{Cu}}^{\text{split}}$  also shows that a study of excess spin density plots may be misleading when analyzing hole localization. While some level of localization can be seen in the excess spin density for both vacancy configurations, it is only through the DOS that the differing magnitudes of hole localization becomes sharply evident, reinforced by the atomic charges from Bader analysis.

The trap level for  $V_{\text{Cu}}^{\text{split}}$  can be compared to the experimentally identified acceptor energy band identified at 0.55–0.61 eV above the VBM.<sup>15</sup> However, the value of the calculated trap level is dependent on how one defines the VBM in the DOS. As evident in the inset of panel c in Figure 3, there is some smearing of the beta spin DOS through the Fermi level,

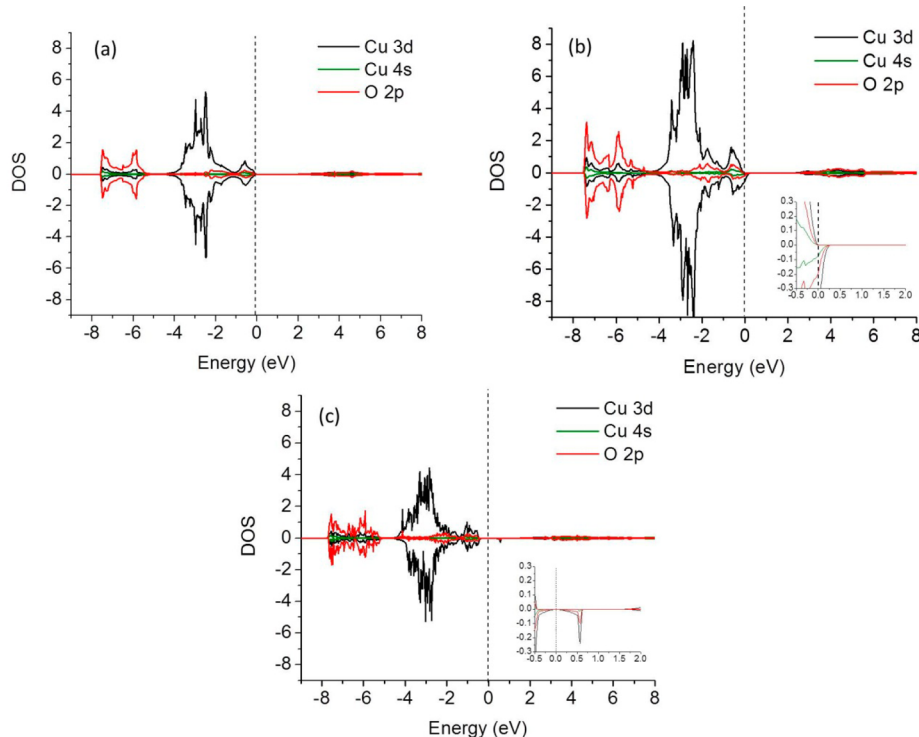


**Figure 3.** Projected DOS for an undoped  $\text{Cu}_2\text{O}$  supercell with (a) no vacancy, (b) a simple vacancy, and (c) a split vacancy, where the alpha (beta) spin DOS are represented by positive (negative) values. The insets in (b) and (c) show the PDOS of the band gap in finer detail. The Fermi level is set to the zero of energy and is represented as a vertical dashed line in all PDOS plots.

making it difficult to define a hard edge to the VBM. We define the VBM to be at the Fermi level, where the beta spin DOS reaches a minimum, resulting in a trap level at 0.57 eV above the VBM. This value agrees well with the experimental results. However, the validity of the comparison may be questionable because the experimental value is derived from absorption experiments, which introduces excitonic effects involving electronic relaxation after excitation. The theoretical model used is a ground state description that does not allow for the band structure to respond to these excited state phenomena, which may be a source of inconsistency between the calculated trap levels and those from experiment. Others have calculated charge transition levels, which can be directly compared to experimental ionization levels from deep level transient spectroscopy, and used them as a metric for XC functional accuracy.<sup>12–14</sup> However, because of the inaccuracies caused by introducing a compensating charged background and the complexity in correcting these errors,<sup>53–55</sup> we chose not to pursue such calculations.

Both defects will exist physically because of the small difference in their formation energies, and therefore, both defects need to be considered when analyzing their effect on photoconductivity. The conditions of preparation of a sample may lead to a “freezing-in” of defects, resulting in a unique type of conductivity at each annealing temperature, where each of the two defect configurations will affect conductivity in dissimilar manners. Although this is not a comprehensive explanation for all experimental phenomena of Cu<sub>2</sub>O conductivity, this provides insight into some of the contributing components to its complexity. The trap states created by split vacancies will enhance minority carrier recombination in the bulk, limiting photoconductivity. On the other hand, simple vacancies lead to delocalized states that will not be detrimental to minority carrier diffusion. It may be possible for a dopant to impact conductivity not only by modifying the defect electronic structure, but also by favoring the formation of one vacancy type over the other. We consider this possibility next.

**B. Vacancies in Doped Cu<sub>2</sub>O.** To accurately model the dopant-vacancy system, it is necessary to identify the optimal configuration for the dopant and vacancy within the supercell. Nolan and Elliot compared the VFEs for two configurations,<sup>40</sup> but in fact seven unique configurations exist, whose unrelaxed initial structures are shown in Figure 4. These initial configurations were constructed with the cation removed to form a simple vacancy, but the defect structure may change after structural optimization. In configurations *a* and *b*, the dopant is located in the same atomic network as the vacancy whereas in configurations *c-g*, the dopant is located in the second atomic network. These configurations vary in their dopant–vacancy distances, also listed in Figure 4. Zn was used as an initial test case, and each configuration’s atomic positions (with lattice vectors fixed at equilibrium values for stoichiometric Cu<sub>2</sub>O) were allowed to relax using PBE+U. VFEs were then calculated with both PBE+U and DFT-HSE. For these DFT-HSE calculations, a smaller k-point set was used in order to decrease the expense of the calculations, sampling an fcc lattice in the Brillouin zone. This sparser k-point sampling was benchmarked against the full k-point mesh for configuration *c*, resulting in an energy difference of 0.04 eV. Because of this minimal energy difference, the use of this k-point mesh is justified when studying trends with DFT-HSE.

The results in Table 6 show that VFEs generally decrease as dopant–vacancy distances decrease, demonstrating a thermo-

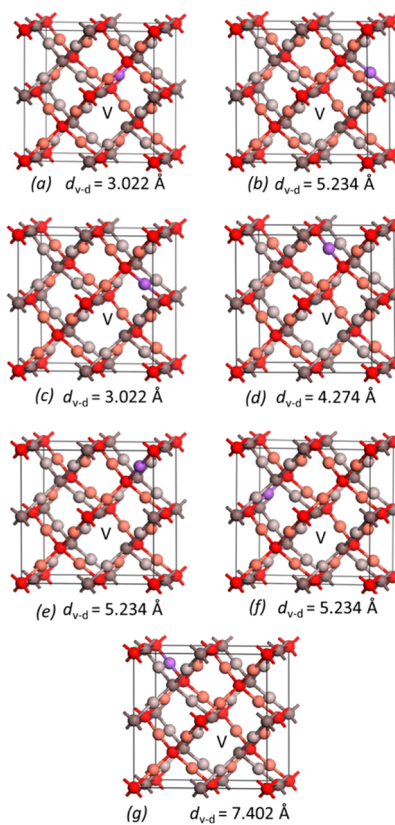


**Figure 4.** Seven unique configurations for dopant and vacancy initial positions within a  $2 \times 2 \times 2$  supercell. One network is indicated with grayed spheres and the other network is indicated with colored spheres, where the red/darker spheres are O and the pink/lighter spheres are Cu. The location of the vacancy is labeled with a “V”, and the dopant atom is shown in purple. The dopant can replace an atom within the same network as the vacancy (configurations *a* and *b*), or can be placed in the other interlocking network (configurations *c-g*). The figures here show initial positions prior to relaxing the structures, and the initial vacancy–dopant distance,  $d_{v-d}$ , is listed below each figure.

**Table 6. Cu VFEs (eV) for Zn-doped Cu<sub>2</sub>O<sup>a</sup>**

dopant/vacancy configuration in Figure 4	vacancy–dopant distance, $d_{v-d}$ (Å)	VFE (eV)	
		PBE+U	DFT-HSE
<i>a</i>	3.022	-0.124	-0.641
<i>b</i>	5.234	0.144	-0.359
<i>c</i>	3.022	-0.823	-1.346
<i>d</i>	4.274	0.042	-0.461
<i>e</i>	5.234	0.022	-0.442
<i>f</i>	5.234	0.022	-0.441
<i>g</i>	7.402	0.187	-0.296

<sup>a</sup>VFEs are presented as a function of dopant position relative to the vacancy, and have been calculated with both PBE+U and DFT-HSE (with a smaller fcc k-point mesh for the latter; see text for details). Values are reported for Cu-rich/O-poor conditions.

dynamic preference to form defect pairs. Although their absolute values differ considerably, both PBE+U and DFT-HSE show the same energy ordering (to within 0.02 eV scatter), indicating that the cheaper PBE+U functional should be reliable for identifying optimal configurations with other dopant elements. Configuration *c* has by far the lowest overall VFE, showing that the optimal configuration is one where the

dopant and vacancy exist in different atomic networks. Configuration *c* was not one of the two studied by Nolan and Elliot, who only sampled configurations corresponding to *a* and *d*.<sup>40</sup> Their reported VFE is significantly higher than the true minimum and their conclusions regarding the dopant's effect on the surrounding structure are questionable, as will be analyzed later.

To verify that configuration *c* is still energetically favored when doping with Li, Mn, and Mg, VFEs for selected configurations were calculated with each of these dopants. Three configurations were sampled: *c*, the most favorable configuration with Zn, to verify that it is still ideal; *a*, the second most energetically favorable configuration, to ensure that the vacancy and dopant still prefer to be situated in different networks; and *g*, the least energetically favorable configuration, to confirm that close proximity is still optimal. Table 7 shows

**Table 7. Cu VFEs (eV) for Configurations *a*, *c*, and *g* When Doped with Li, Mg, Mn, and Zn, as Calculated with PBE+U, for Cu-Rich/O-Poor Conditions**

configuration	Li-doped	Mg-doped	Mn-doped	Zn-doped
<i>a</i>	1.302	-0.076	-0.108	-0.124
<i>c</i>	0.769	-1.589	-1.166	-0.823
<i>g</i>	1.121	0.139	0.152	0.187

these VFEs calculated with PBE+U, and it is evident that configuration *c* is still the most stable. The energy difference between vacancy formation proximal to the dopant (*c*) and vacancy formation far from the dopant (*g*) is significant, with a difference of 0.35, 1.73, 1.32, and 1.01 eV for Cu<sub>2</sub>O doped with Li, Mg, Mn, and Zn, respectively. This driving force to promote clustering of the dopant and vacancy suggests that dopants will have a strong impact on the vacancy and its resulting electronic structure. (If it would have been energetically favorable to form vacancies far from the dopant, the dopant would be less likely to interact with the vacancy, and the vacancy's properties would be nearly the same as those in pure Cu<sub>2</sub>O.) Although it is still possible for other configurations to exist in much lower concentrations, this configuration (*c*) will certainly be the dominant defect, and is thus the configuration that will be explored in all further calculations.

For a final evaluation of VFEs, DFT-HSE calculations were done with the larger 2 × 2 × 2 k-point and q-point mesh. Table 8 shows these values in comparison with the undoped formation energies, for both environmental limits. The effect of all n-type dopants is to stabilize the vacancy and significantly lower the VFE, a trend consistent with the observation of

**Table 8. Cu VFEs (eV) for Doped (in configuration *c*) and Pure Cu<sub>2</sub>O, under Cu-Rich/O-Poor and Cu-Poor/O-Rich Conditions, as Calculated with DFT-HSE with a Full 2 × 2 × 2 k-point Mesh**

dopant	Cu VFE (eV)	
	Cu-rich/O-poor	Cu-poor/O-rich
Li	1.102	0.918
Mg	-2.228	-2.412
Mn	-1.341	-1.526
Zn	-1.389	-1.573
undoped, simple vacancy	1.337	1.152
undoped, split vacancy	1.580	1.396

Nolan and Elliot.<sup>40</sup> Doping isovalently with Li also lowers the VFE slightly. Vacancy stabilization by n-type dopants is partially due to the extra electron compensating the hole introduced in vacancy formation. However, if charge compensation was the only source of vacancy stabilization, there would be no variation in the VFEs of Tables 6 and 7, because charge compensation occurs in each configuration. Therefore, it is evident that defect structural changes also play a significant role in reducing the VFEs, an effect that can be isolated when doping with Li. These dopants typically have a minimum coordination number of four in most materials. However, when incorporated into Cu<sub>2</sub>O without a vacancy, they are forced to conform to the coordination of Cu in the bulk, which is two. A nearby cation vacancy allows the dopant to move to a position that will allow it to obtain its preferred coordination of four, stabilizing the dopant. The final configuration is similar to that of V<sub>Cu</sub><sup>split</sup>, where the dopant atom is tetrahedrally coordinated to four nearby O atoms. This final relaxed structure is shown for the Zn-doped cell in Figure 5, and this geometry is consistent with that of all

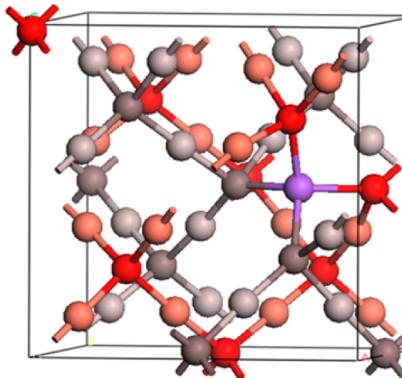


**Figure 5.** Relaxed structure for the Zn-doped Cu<sub>2</sub>O supercell with a Cu cation vacancy, showing the tetrahedral coordination of Zn. One network is indicated with grayed spheres and the other network is indicated with colored spheres, where the red/darker spheres are O and the pink/lighter spheres are Cu. Zn is shown in purple.

other dopants. The stabilization of the dopant via reorganization contributes significantly to the lowering of the VFE. The VFE reduction by n-type dopants explains why it is so difficult to create n-type Cu<sub>2</sub>O. Although n-type dopants introduce excess electrons, they also promote vacancy formation, generating extra holes that compensate the charges of the additional electrons.

One question arises from the previous observation regarding the optimal structure. This tetrahedrally coordinated dopant configuration was found to be the most stable when relaxing from the starting configuration of a simple vacancy with a nearby dopant (configuration *c*); however, it is unknown if another configuration might be found to be more stable when starting from a different initial structure. Specifically, could it be preferable for the vacancy to exist in a V<sub>Cu</sub><sup>split</sup> structure with the dopant atom acting as a neighboring spectator? Figure 6 shows how to construct such a defect starting from configuration *c*, where four unique configurations can be created: the first is identical to the optimal configuration identified previously, and the other three assume a V<sub>Cu</sub><sup>split</sup> structure. We tested the stability of these four configurations with each of the four dopants, and atomic positions were relaxed from these initial configurations using PBE+U. It was found that no matter the starting

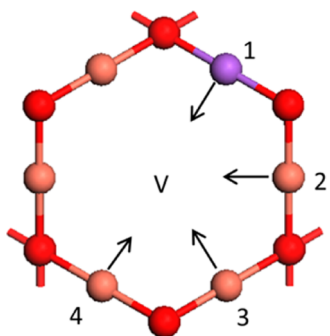


**Figure 6.** Nearest neighbors around a Cu vacancy in  $\text{Cu}_2\text{O}$ , labeled “V”, showing the local geometry of configuration c. There are four unique ways to construct a split vacancy when beginning with this structure, each indicated by an arrow: moving the dopant atom from position 1 toward the vacancy, or moving a Cu atom from positions 2–4 toward the vacancy.

geometry, the relaxed structure consistently had the dopant tetrahedrally coordinated to four O atoms, verifying that this is indeed the global minimum. This exercise additionally shows that the presence of a dopant will prevent  $V_{\text{Cu}}^{\text{split}}$  formation, a beneficial side effect on the electronic structure that will be discussed further. The relaxed structure, with its tetrahedral coordination of the dopant, is a significant deviation from the stoichiometric lattice. This is in contrast with the observations of Nolan and Elliot, who reported that the Zn-doped structure does not vary significantly from the native structure and exists with a vacancy in the form of  $V_{\text{Cu}}^{40}$ . Their observation was an unfortunate consequence of studying a structure that did not allow for the ideal dopant configuration. As a result, they missed the impact the dopant has on the  $\text{Cu}_2\text{O}$  structure after vacancy formation.

To analyze hole localization, the excess spin density can be plotted only for Li-doped, defective  $\text{Cu}_2\text{O}$ , as n-type-doped, defective  $\text{Cu}_2\text{O}$  has an even number of electrons and it is not possible to isolate the hole spin density. Figure 7 shows the excess spin density for the Li-doped supercell, with the isosurface level set to half of the maximum density ( $0.032 \text{ e} \text{ \AA}^{-3}$ ). This figure shows slight localization of the hole on two of the  $\text{Cu}_{\text{NNN}}$  atoms, but a lower isosurface threshold (not shown) shows further delocalization of the hole on the atoms

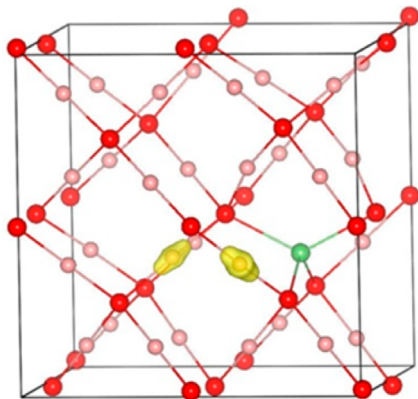


**Figure 7.** Excess spin density for Li-doped  $\text{Cu}_2\text{O}$  with a Cu vacancy, as calculated with DFT-HSE. The red, pink, and green spheres represent O, Cu, and Li, respectively. The isosurface level is set to half of the maximum density, at  $0.032 \text{ e} \text{ \AA}^{-3}$ .

surrounding the defect. This observation was further validated through Bader analysis of the charge distribution discussed next.

The extent of hole localization near the vacancy is revealed in Table 9, which lists the Bader charges for doped  $\text{Cu}_2\text{O}$  with no vacancy compared to those for doped  $\text{Cu}_2\text{O}$  containing a vacancy. The charges for doped  $\text{Cu}_2\text{O}$  with a vacancy include the extra hole added via vacancy formation, and by analyzing the charge differential, one can identify this additional hole’s location. The Bader charges on Li and Mg remain consistent in both systems and correspond to a formal charge of +1 for Li and +2 for Mg, their most stable oxidation states. When a vacancy is formed in these two systems, the hole delocalizes among other atoms, with a slightly more significant increase in positive charge observed on two of the  $\text{Cu}_{\text{NNN}}$  atoms close to the Li or Mg dopant. Conversely, for Mn and Zn, the changes in Bader charges show that the added hole is quite strongly localized on the dopant atom, which changes oxidation state accordingly. This reflects the ability of transition metals to exist stably in multiple oxidation states, in contrast with alkali and alkaline earth metals. Adding a hole to  $\text{Li}^+$  or to  $\text{Mg}^{2+}$  corresponds to ionizing a core electron, which is energetically very costly, whereas adding a hole to  $\text{Mn}^{2+}$  or  $\text{Zn}^{2+}$  corresponds to ionizing a valence d-electron, which costs less energy and therefore can more readily occur. The localization of the added hole on Mn and Zn illustrates the compensatory effect of the added hole, which has combined with the additional electron contributed by and previously localized on these n-type dopants.

Although hole localization is evident via Bader analysis, this does not unequivocally signify the existence of a trap state, especially when accounting for charge compensation. Rather, it is necessary to examine the DOS of these materials to fully understand the effect of the dopant on the electronic structure. Figure 8 shows projected DOS for doped  $\text{Cu}_2\text{O}$  with a cation vacancy. All plots clearly indicate that there are no states within the gap. Thus, these dopants prevent the creation of trap states from a single Cu vacancy, which can be explained via two different effects. First, these dopants prevent formation of  $V_{\text{Cu}}^{\text{split}}$ , which creates midgap trap states. Second, charge compensation by n-type dopants allow for the hole to be localized on the dopant without creating a deleterious acceptor state or prevent its localization on any single atom completely. By preventing the formation of acceptor states, dopants may help to improve minority carrier transport and inhibit recombination in the bulk, enhancing  $\text{Cu}_2\text{O}$  as a material for photocatalytic and photovoltaic applications. Because dopant-vacancy clustering is significantly energetically favorable, the impact of these dopants on a single vacancy will be substantial. This conclusion is definitive for the iso-vaalent dopant Li, whose effect on conductivity can be analyzed by its impact on a single vacancy. However, in order to truly analyze the full effect of n-type dopants on photoconductivity, it is necessary to study the impact of these dopants on a second hole that does not undergo charge compensation. Therefore, the following section studies the effect of all n-type dopants on a second cation vacancy.

**C. Two Vacancies in n-Type  $\text{Cu}_2\text{O}$ .** When modeling  $\text{Cu}_2\text{O}$  with two vacancies, it is necessary to use the larger ( $3 \times 3 \times 3$ ) supercell to maintain a physically reasonable concentration of vacancies (~2.5%). However, at that cell size, it becomes computationally impossible to use DFT-HSE to study the electronic structure, which is crucial for an accurate analysis of

**Table 9. Bader Charges of Doped Cu<sub>2</sub>O without (with) a Cation Vacancy<sup>a</sup>**

atom	stoichiometric Cu <sub>2</sub> O	Li-doped	Mg-doped	Mn-doped	Zn-doped
O <sub>NN</sub>		-1.22 (-1.15)	-1.28 (-1.23)	-1.17 (-1.18)	-1.17 (-1.17)
O <sub>bulk</sub>	-1.11	-1.12 (-1.14)	-1.11 (-1.14)	-1.11 (-1.13)	-1.11 (-1.14)
Cu <sub>NN</sub>		0.56 (0.56)	0.54 (0.53)	0.56 (0.54)	0.54 (0.55)
Cu <sub>NNN</sub>		0.56 (0.59)	0.48 (0.57)	0.52 (0.57)	0.52 (0.57)
Cu <sub>bulk</sub>	0.55	0.55 (0.58)	0.55 (0.57)	0.55 (0.57)	0.55 (0.57)
M		0.86 (0.88)	1.57 (1.68)	0.95 (1.43)	0.98 (1.32)

<sup>a</sup>Bader charges for doped Cu<sub>2</sub>O without and with a cation vacancy, as calculated with DFT-HSE, averaged for classes of atom types. Values in parentheses present Bader charges for the cell containing a vacancy. Bader charges for bulk Cu and O can be compared to the bulk charges in stoichiometric Cu<sub>2</sub>O, shown in the second column. For cells without (with) a vacancy, M is the dopant atom, and other atom classes are defined in the same manner as the relative positions of atoms to the vacancy in  $V_{\text{Cu}}(V_{\text{Cu}}^{\text{split}})$ , as shown in Figure 2. In the cases with no vacancy, the dopant atom resides in the position where the simple vacancy would have been.

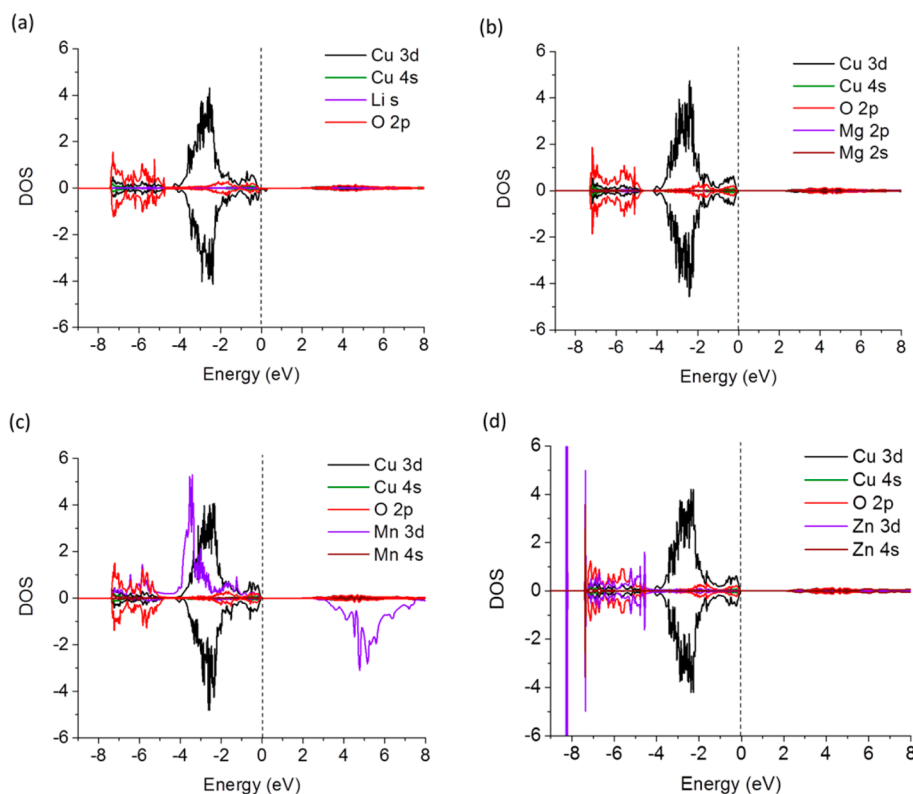


**Figure 8.** Projected DOS for Cu<sub>2</sub>O with a Cu vacancy, substitutionally doped with (a) Li, (b) Mg, (c) Mn, and (d) Zn in the configuration depicted in Figure 5.

the density of states. Therefore, we first determined the optimal configuration of the dopant and vacancies within the (3 × 3 × 3) supercell using PBE+U. If the lowest-energy configuration has a large vacancy–vacancy distance, it is likely that the dopant will have a minimal impact on the second vacancy, and the energetics and electronic structure resulting from this second vacancy will be nearly identical to the pure material. Alternatively, if the lowest-energy configuration has a small vacancy–vacancy distance, the dopant may significantly impact the electronic structure resulting from the second vacancy. However, the overall impact of the dopant will depend on the driving force to cluster the defect. If there is a small energy difference between the second VFE near and far from the dopant, then the dopant will only minimally impact conductivity, as vacancies (both simple and split) will still readily form far from it. Finally, if the optimal defect is a localized cluster of the vacancies and dopants, we can study the local impact of the dopant with the smaller (2 × 2 × 2) cell,

facilitating the use of DFT-HSE for more accurate electronic structure calculations.

Six defect configurations within the (3 × 3 × 3) supercell were sampled. The dopant and the first vacancy will likely arrange similarly to the lowest energy configuration for a dopant with a single vacancy, so the position of the second vacancy becomes the only variable when creating the initial structure prior to relaxation. Figure 9 shows these six initial configurations, where the position of the second vacancy varies in its distance to the dopant, its distance to the first vacancy, and its location in one of the two atomic networks. The values of these parameters are also presented in Table 10, reflecting the initial arrangements of these structures prior to relaxation with PBE+U. Although more configurations may exist in this system, these six configurations were chosen to sample representative values of these parameters.

After structural optimization, the formation enthalpy of the second vacancy was calculated for each of the n-type doped

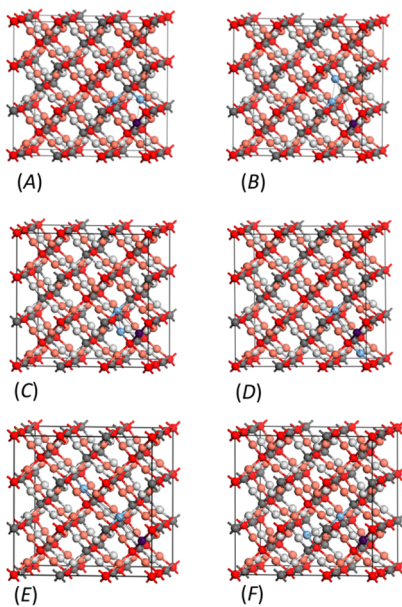


**Figure 9.** The six sampled configurations of two vacancies and one dopant within a  $(3 \times 3 \times 3)$  supercell. One network is indicated with grayed spheres and the other with colored spheres, where the red/darker spheres are O, the pink/lighter spheres are Cu, and the deep purple sphere is the n-type dopant. For clarity in the spatial orientation, the Cu vacancies are represented by light blue spheres. These six configurations differ by their distances between dopant and vacancies as well as in the networks in which the vacancies exist, whose values are listed in Table 10.

supercells with PBE+U (Table 10). Configurations A or C have the lowest second VFE for the Mg and Mn dopants, with C also lowest for Zn, showing that the VFE is minimized when the two vacancies and dopant are allowed to be in close proximity. The preferred clustering of the defect structure indicates that the second vacancy's electronic structure will differ from that of a vacancy in undoped  $\text{Cu}_2\text{O}$ . However, the potential impacts of these n-type dopants on photoconductivity are largely dependent on the ability of these dopants to promote clustering to form the defect complex. The VFEs in Table 10 show that the energy gained from clustering is below 0.1 eV in most cases. This is in contrast with the larger decrease in energy associated with the formation of a localized dopant-vacancy complex with the first vacancy, shown in Tables 6 and 7. Therefore, although all n-type dopants have a strong effect on formation of the first

vacancy, the effect on the second vacancy is much smaller. These results suggest that n-type dopants may only minimally impact photoconductivity unless present at high dopant concentrations.

This conclusion inherently assumed that a clustered defect complex with a split vacancy is higher in energy than one with a simple vacancy (configuration C in Figure 9) and therefore split vacancy formation does not play a large role in promoting defect clustering. To test this assumption, the initial structure from configuration C was perturbed and subsequently relaxed to create new structures with split vacancies (denoted  $\text{C}-\text{V}_{\text{Cu}}^{\text{split}}$ ). The second VFEs for the lowest energy  $\text{C}-\text{V}_{\text{Cu}}^{\text{split}}$  structures are shown in the final row of Table 10. All structures with a split vacancy were found to be higher in energy than configuration C, and therefore considering the split vacancy does not change the initial conclusion regarding the minimal impact of n-type dopants on photoconductivity.

Finally, to better understand the impact of the dopant on the electronic structure in the clustered defect complex, one may turn to DFT-HSE, which necessitates modeling the system with the smaller  $(2 \times 2 \times 2)$  cell. This will provide a localized description of the impact of the dopant on the second vacancy, which is an approximation to the larger  $(3 \times 3 \times 3)$  cell. However, because these calculations will not change the established conclusion that the dopant will only minimally impact the second vacancy, these results are reported in the Supporting Information. There we show that Mn as a dopant may worsen  $\text{Cu}_2\text{O}$  photoconductivity, as it decreases the formation energy for defects that introduce trap states, whereas Zn shows potential for improvement at high dopant concentrations.

#### 4. CONCLUSIONS

Simple and split cation vacancies in  $\text{Cu}_2\text{O}$  were studied using DFT-GGA (PBE), PBE+U theory, and hybrid DFT (HSE). It was found that the simple vacancy was consistently more stable than the split vacancy by  $0.21 \pm 0.03$  eV, regardless of the exchange-correlation functional used. DFT-HSE was then used to study the electronic structure, as it was shown previously to provide the most accurate properties of stoichiometric  $\text{Cu}_2\text{O}$ .<sup>45</sup> The simple vacancy exhibits a delocalized hole with states smeared through the Fermi level, whereas the split vacancy displayed a discrete trap state 0.57 eV above the Fermi level, indicative of a localized hole. Bader analysis validated these observations, showing that the hole in the split vacancy is

**Table 10. Second Cu VFEs (eV) in a  $(3 \times 3 \times 3)$  Supercell Doped with Mg, Mn, and Zn<sup>a</sup>**

Conf.	which network?			unrelaxed distances (Å)			second Cu VFE (eV)		
	d	v1	v2	$d_{\text{d-v1}}$	$d_{\text{d-v2}}$	$d_{\text{v1-v2}}$	Mg-doped	Mn-doped	Zn-doped
A	1	2	2	3.022	3.022	3.022	1.010	0.969	1.161
B	1	2	2	3.022	5.234	3.022	1.197	1.185	1.094
C	1	2	1	3.022	3.022	3.022	1.012	0.969	1.018
D	1	2	1	3.022	3.022	5.234	1.196	1.180	1.093
E	1	2	2	3.022	10.023	7.996	1.130	1.106	1.125
F	1	2	1	3.022	9.066	7.996	1.111	1.088	1.110
$\text{C}-\text{V}_{\text{Cu}}^{\text{split}}$	1	2	1	3.022	3.022	3.022	1.090	1.017	1.143

<sup>a</sup>VFEs (eV) for a second vacancy in configurations of a  $(3 \times 3 \times 3)$  supercell doped with Mg, Mn, and Zn, as calculated with PBE+U and reported for Cu-rich/O-poor conditions. The initial structures of six configurations (A–F) prior to relaxation are defined by the locations of the unrelaxed dopant (d) and vacancies (v1, v2) in atomic network 1 or 2, the distances between the dopant and each vacancy ( $d_{\text{d-v1}}$ ,  $d_{\text{d-v2}}$ ), and the distance between the two vacancies ( $d_{\text{v1-v2}}$ ). The final configuration ( $\text{C}-\text{V}_{\text{Cu}}^{\text{split}}$ ) is where the relaxed structure from configuration C was perturbed to create a split vacancy.

localized on the Cu atom central to the defect, whereas negligible hole localization occurs on atoms surrounding the simple vacancy. Because of the small difference in VFEs of the two defect geometries, both are expected to exist in undoped samples, and both will contribute to electronic conductivity via differing mechanisms. Specifically, the split vacancy will create defect-localized-states in the gap that have an associated activation energy to contribute to p-type semiconduction, while the simple vacancy results in holes occupying perturbed-hole-states that readily contribute to p-type semiconduction with no associated activation energy.

Use of a converged k-point mesh was shown to have a significant impact on the results of DFT-HSE calculations, as insufficient k-point sampling led to predictions of localized holes with discrete acceptor states in the gap for both vacancy types. Our results prompt a reevaluation of conclusions previously reached by Scanlon et al.<sup>14</sup> and underscore the importance of using well-converged computational parameters to ensure that even qualitative conclusions are on firm footing.

The split vacancy was identified as the source of trap states that inhibit minority carrier diffusion. Doping with Li, Mg, Mn, and Zn prevented the formation of split vacancies for a single cation vacancy, resulting in an electronic structure that exhibited no trap states within the band gap. The addition of the dopant affected hole localization, as the additional hole from a single vacancy was delocalized in Cu<sub>2</sub>O doped with Li and Mg, but was at least partially localized on the dopant when doped with Mn and Zn, which can be understood in terms of the relative magnitudes of the relevant ionization potentials of these cations. The optimal single-vacancy defect structure was identified to be one in which the dopant is tetrahedrally coordinated to four oxygen atoms, similar to the structure of a split vacancy. It is crucial that this optimal configuration be used when modeling doped Cu<sub>2</sub>O with a single cation vacancy. This configuration allows the dopant to exist with its natural tetrahedral coordination, resulting in a large driving force to cluster the dopant and vacancy. These dopants will therefore have a strong impact on a single vacancy, suggesting that the isovalent dopant, Li, has the potential to improve photoconductivity. In contrast, the ability of the charge compensating Mg, Mn, and Zn dopants to improve photoconductivity will be limited by their ability to promote clustering of a second simple vacancy with the dopant. Because clustering here is only minimally energetically favorable, the contributions of these dopants to improve photoconductivity will be small, unless dopant concentrations near that of the vacancies can be achieved. At high dopant concentrations, Mn will promote the formation of trap states and be detrimental to photoconductivity, whereas Zn may slightly inhibit the formation of trap states to improve photoconductivity.

Our results illustrate the potential beneficial impact that Li could have on the photoconductivity of Cu<sub>2</sub>O, by greatly suppressing formation of split vacancies that are probably the originators of trap states in this material. While these calculations were performed at relatively high dopant and vacancy concentrations due to computational limits on supercell size, our analysis is of local effects whose consequences should be relevant to a range of concentrations.

## ASSOCIATED CONTENT

### Supporting Information

Ionic radii of dopants in comparison with Cu<sup>+</sup>, verification of the stability of V<sub>Cu</sub> and V<sub>Cu</sub><sup>split</sup> through an analysis of vibrational

frequencies, evaluation of structural disruption of vacancy formation, a study of the effect of total magnetization of Mn-doped Cu<sub>2</sub>O, and calculations of two vacancies in a (2 × 2 × 2) supercell for n-type Cu<sub>2</sub>O. This material is available free of charge via the Internet at <http://pubs.acs.org/>.

## AUTHOR INFORMATION

### Corresponding Author

\*Fax: +1 609 258 5877. E-mail: eac@princeton.edu.

### Notes

The authors declare no competing financial interest.

## ACKNOWLEDGMENTS

E.A.C. acknowledges the support of the Air Force Office of Scientific Research and the Department of Energy, Basic Energy Sciences, for funding and the DoD High Performance Computing Modernization Program at the NAVY, AFRL, and ERDC DSRC for supercomputer resources. L.Y.I. acknowledges support as a National Science Foundation Graduate Fellow and thanks Andrew Ritzmann for providing the converged first principles data for the O<sub>2</sub> molecule.

## REFERENCES

- (1) Brahms, S.; Nikitine, S.; Dahl, J. P. *Phys. Lett.* **1966**, *22*, 31.
- (2) Rai, B. P. *Sol. Cells* **1988**, *25*, 265.
- (3) Hara, M.; Kondo, T.; Komoda, M.; Ikeda, S.; Kondo, J. N.; Domen, K.; Hara, M.; Shinohara, K.; Tanaka, A. *Chem. Commun.* **1998**, 357.
- (4) Jongh, P. E. de; Vanmaekelbergh, D.; Kelly, J. J. *J. Chem. Commun.* **1999**, 1069.
- (5) Papadimitriou, L.; Dimitriadis, C. A.; Dozsa, L. *Solid-State Electron.* **1988**, *31*, 1477.
- (6) Porat, O.; Riess, I. *Solid State Ionics* **1995**, *81*, 29.
- (7) Porat, O.; Riess, I. *Solid State Ionics* **1994**, *74*, 229.
- (8) Xue, J.; Dieckmann, R. *J. Phys. Chem. Solids* **1990**, *51*, 1263.
- (9) Yoshimura, M.; Revcolevschi, A.; Castaing, J. *J. Mater. Sci.* **1976**, *11*, 384.
- (10) Mrowec, S.; Stoklosa, A.; Godlewski, K. *Cryst. Latt. Def.* **1974**, *5*, 239.
- (11) Soon, A.; Cui, X.-Y.; Delley, B.; Wei, S.-H.; Stampfli, C. *Phys. Rev. B* **2009**, *79*, 035205.
- (12) Raebiger, H.; Lany, S.; Zunger, A. *Phys. Rev. B* **2007**, *76*, 045209.
- (13) Scanlon, D. O.; Morgan, B. J.; Watson, G. W. *J. Chem. Phys.* **2009**, *131*, 124703.
- (14) Scanlon, D. O.; Morgan, B. J.; Watson, G. W.; Walsh, A. *Phys. Rev. Lett.* **2009**, *103*, 096405.
- (15) Zouaghi, M.; Prevot, B.; Carabatos, C.; Sieskind, M. *Phys. Status Solidi A* **1972**, *11*, 449.
- (16) Tretyakov, Y. D.; Komarov, V. F.; Prosvirnina, N. A.; Kutsenok, I. B. *J. Solid State Chem.* **1972**, *5*, 157.
- (17) Aggarwal, S.; Töpfer, J.; Tsai, T.-L.; Dieckmann, R. *Solid State Ionics* **1997**, *101*, 321.
- (18) O'Keeffe, M.; Moore, W. J. *J. Chem. Phys.* **1961**, *35*, 1324.
- (19) Brattain, W. H. *Rev. Mod. Phys.* **1951**, *23*, 203.
- (20) Tapiero, M.; Zielinger, J. P.; Noguet, C. *Phys. Status Solidi A* **1972**, *12*, 517.
- (21) Meyer, W.; Neldel, H. Z. *Tech. Phys.* **1937**, *18*, 588.
- (22) Noguet, C.; Tapiero, M.; Zielinger, J. P. *Phys. Status Solidi A* **1974**, *24*, S65.
- (23) Kužel, R. *Czech. J. Phys.* **1958**, *8*, 81.
- (24) Klier, É.; Kužel, R.; Pastrnák, J. *Czech. J. Phys.* **1955**, *5*, 421.
- (25) Kužel, R. *Czech. J. Phys.* **1961**, *11*, 133.
- (26) Kužel, R. *Czech. J. Phys.* **1965**, *15*, 709.
- (27) Tapiero, M.; Zielinger, J. P.; Noguet, C. *Phys. Status Solidi A* **1976**, *33*, 155.

- (28) Zielinger, J. P.; Noguet, C.; Tapiero, M. *Phys. Status Solidi A* **1977**, *42*, 91.
- (29) Wright, A. F.; Nelson, J. S. *J. Appl. Phys.* **2002**, *92*, 5849.
- (30) Nolan, M.; Elliott, S. D. *Phys. Chem. Chem. Phys.* **2006**, *8*, 5350.
- (31) Persson, C.; Zhao, Y.-J.; Lany, S.; Zunger, A. *Phys. Rev. B* **2005**, *72*, 035211.
- (32) Anisimov, V. I.; Zaanen, J.; Andersen, O. K. *Phys. Rev. B* **1991**, *44*, 943.
- (33) Dudarev, S. L.; Liechtenstein, A. I.; Castell, M. R.; Briggs, G. A. D.; Sutton, A. P. *Phys. Rev. B* **1997**, *56*, 4900.
- (34) Heyd, J.; Scuseria, G. E.; Ernzerhof, M. *J. Chem. Phys.* **2003**, *118*, 8207.
- (35) Heyd, J.; Scuseria, G. E. *J. Chem. Phys.* **2004**, *120*, 7274.
- (36) Heyd, J.; Scuseria, G. E. *J. Chem. Phys.* **2004**, *121*, 1187.
- (37) Tang, W.; Sanville, E.; Henkelman, G. *J. Phys.: Condens. Matter* **2009**, *21*, 084204.
- (38) Papadimitriou, L. *Solid State Commun.* **1989**, *71*, 181.
- (39) Nolan, M.; Elliott, S. D. *Thin Solid Films* **2008**, *516*, 1468.
- (40) Nolan, M.; Elliott, S. D. *Chem. Mater.* **2008**, *20*, 5522.
- (41) Perdew, J. P.; Burke, K.; Ernzerhof, M. *Phys. Rev. Lett.* **1996**, *77*, 3865.
- (42) Perdew, J. P.; Burke, K.; Ernzerhof, M. *Phys. Rev. Lett.* **1997**, *78*, 1396.
- (43) Liao, P.; Carter, E. A. *Chem. Soc. Rev.* **2012**, in press.
- (44) Shannon, R. D. *Acta Crystallogr. A* **1976**, *32*, 751.
- (45) Isseroff, L. Y.; Carter, E. A. *Phys. Rev. B* **2012**, *85*, 235142.
- (46) Kresse, G.; Joubert, D. *Phys. Rev. B* **1999**, *59*, 1758.
- (47) Blöchl, P. E. *Phys. Rev. B* **1994**, *50*, 17953.
- (48) Dudarev, S. L.; Botton, G. A.; Savrasov, S. Y.; Humphreys, C. J.; Sutton, A. P. *Phys. Rev. B* **1998**, *57*, 1505.
- (49) Krukau, A. V.; Vydrov, O. A.; Izmaylov, A. F.; Scuseria, G. E. *J. Chem. Phys.* **2006**, *125*, 224106.
- (50) Blöchl, P. E.; Jepsen, O.; Andersen, O. K. *Phys. Rev. B* **1994**, *49*, 16223.
- (51) Lide, D. R. *CRC Handbook of Chemistry and Physics 2012–2013*; CRC Press: Boca Raton, FL, 2012.
- (52) Lany, S.; Zunger, A. *Phys. Rev. B* **2005**, *72*, 035215.
- (53) Makov, G.; Payne, M. C. *Phys. Rev. B* **1995**, *51*, 4014.
- (54) Komsa, H.-P.; Rantala, T. T. *arXiv:0906.1283* **2009**.
- (55) Lento, J.; Mozos, J.-L.; Nieminen, R. M. *J. Phys.: Condens. Matter* **2002**, *14*, 2637.
- (56) Straumanis, M. E.; Yu, L. S. *Acta Crystallogr., Sect. A* **1969**, *25*, 676.
- (57) Ledbetter, H. M.; Naimon, E. R. *J. Phys. Chem. Ref. Data* **1974**, *3*, 897.